Aerodynamic Database Generation for SRB Separation from a Heavy Lift Launch Vehicle

Marshall R. Gusman* and Michael F. Barad†
Science and Technology Corporation, Moffett Field, CA 94035
Cetin C. Kiris‡
NASA Ames Research Center, Moffett Field, CA 94035

An engineering approach is presented for database generation of aerodynamic force and moment coefficients on Solid Rocket Boosters (SRBs) during separation from a Heavy Lift Launch Vehicle. The approach balances accuracy and affordability by generating a steady-state database of solutions using the inviscid flow solver Cart3D with adjoint based adaptive mesh refinement. The procedure also includes point checking the database using the viscous Reynolds Averaged Navier-Stokes solver OVERFLOW. The simulation matrix consists of 3 degrees of freedom by planar translation and rotation of the SRBs from their original attached positions. Good agreement with viscous multi-species simulations has confirmed that the single-species inviscid assumptions are valid for this plume impingement flow. The database provides axial forces, side forces, and yaw moments on the SRBs during separation from the core. This data is to be used for vehicle and trajectory planning to avoid re-contacting the core.

Nomenclature

β	Rotation angle (degrees)	HLLV	Heavy Lift Launch Vehicle
γ	Ratio of specific heats	M	Mach number
Δx	Translation downstream (normalized)	P	Pressure (Pa)
Δy	Translation cross-stream (normalized)	SRB	Solid Rocket Booster
ρ	Density (kg/m^3)	V	Velocity (m/s)
A	Area of nozzle cross-section (m^2)	c	Speed of sound (m/s)
CA	Axial force coefficient	CG	Center of Gravity
CLN	Yaw moment coefficient	CY	Side force coefficient
F&M	Force and Moment		

I. Introduction

The National Aeronautics and Space Administration (NASA) is currently exploring options for future Heavy Lift Launch Vehicles (HLLV) to carry large payloads to low-earth-orbit and beyond. Computational Fluid Dynamics (CFD) simulations have been established as a central component in the performance evaluation of launch vehicles during lift-off and throughout the mission, see Kiris et al.[1] and Gomez et al.[2] In particular, databases of aerodynamic forces and moments (F&M) have been generated for HLLVs with and without plumes, with extensive sensitivity studies, code-to-code comparisons, and validation with experiments and flight data, see Kiris et al.[3] and Gusman et al.[4]

*Research Scientist, Applied Modeling and Simulation Branch, NAS Division, MS N258-2; Marshall.R.Gusman@nasa.gov.
†Research Scientist, Applied Modeling and Simulation Branch, NAS Division, MS N258-2; Michael.F.Barad@nasa.gov.
‡Branch Chief, Applied Modeling and Simulation Branch, NAS Division, MS N258-2; Cetin.C.Kiris@nasa.gov.

The HLLV under present consideration is composed of a core stage with 5 liquid-fueled RS-68 rocket engines and two Solid Rocket Boosters (SRBs). Approximately 120 seconds after lift-off, the solid fuel is mostly spent and the SRBs are jettisoned from the core stage. An understanding of the flow physics during this separation maneuver is necessary for proper sizing of the separation motors, in order to avoid re-contact with the core stage.

The aim of this work is to develop an accurate and efficient methodology for studying HLLV stage-separation. During the early stages of the HLLV development effort, the vehicle configuration and launch trajectory are continually changing. In this situation, solution fidelity must be balanced with efficient turn-around time for CFD to impact design decisions. To address the need for relatively fast and reasonably accurate database generation, the assumptions of inviscid and single-species flow are used to reduce the problem's complexity. The computational requirements for an inviscid single-species flow solution using Cart3D are approximately 2 orders of magnitude less than a viscous multi-species solution using OVERFLOW. The reduced resource requirements allow a much more comprehensive trajectory matrix to be explored in a shorter amount of time. Selected points in the trajectory are chosen to compare with results from the higher-fidelity viscous flow solver to assess the implications of the inviscid single-species assumptions.

A detailed problem description follows, with explanations of the simulation matrix and nozzle boundary conditions. Next, the computational method is outlined for both inviscid and viscous codes. The results are analyzed to identify trends and important aspects of stage-separation. Finally, solution comparisons between Cart3D and OVERFLOW at select points in the trajectory are examined.

II. Problem Description

An understanding of the forces and moments acting on the SRBs during separation is necessary to size the separation motors, plan the separation trajectory, and assess mission risk. The dominant aerodynamic influences on the SRBs are the incoming free-stream flow (after passing through the core stage bow shock), and the core stage main engine exhaust plumes. At the time of separation, the low-pressure ambient environment causes significant plume expansion that will impinge on the SRBs as they separate. A large force on the rear portion of an SRB will cause a rotational moment, with the potential for re-contacting the core stage. Due to jet impingement and relative body motion the physics of SRB separation is inherently unsteady. Separation dynamics can be approximated by a sequence of independent steady-state runs.[5,6] The aerodynamic forces and moments experienced by the SRBs during separation are computed using a database of steady-state flow solutions performed at fixed increments through three possible separation trajectories.

CFD Simulation Matrix

Figure 1(a) illustrates the notation for translation and rotation of SRBs. Downstream translation is denoted by Δx and sideways translation by Δy, where Δx and Δy are normalized by their respective maximum values. A positive angle $+\beta$ will rotate the SRB nose-away from the core, and about its center of gravity (CG). In the nominal separation trajectory, the SRBs move out and away from the core stage in a roughly parabolic path. This path is shown in red in Figure 1(b). The minimum-Δy trajectory passes directly downstream from the SRBs' initial positions; negative Δy translation being limited by re-contact, or intersection, with the core stage. The maximum-Δy trajectory is roughly double the nominal trajectory, except near Δx =0 where it accounts for a sideways separation. To thoroughly cover the potential separation trajectories, a simulation matrix is created with seven Δy locations spanning the minimum, nominal, and maximum trajectories for each Δx location. Locations for Δx are every 0.025 up to 0.5, and every 0.05 up to a maximum 1.0 downstream, for a total of 31 Δx translations. For every translation combination, rotations of 0, $\pm$2, $\pm$4, $\pm$6, and $\pm$8 degrees are considered. The total number of configurations is 1953. For 269 of the combinations, the rotated SRBs intersect with the core stage. Simulations of these orientations are not attempted, so the final simulation matrix contains 1684 unique SRB orientations. All simulations were conducted at Mach and Reynolds numbers corresponding to the flight condition at time of SRB separation.

Nozzle Boundary Conditions

Two nozzle boundary condition approaches are used in this study. For the OVERFLOW simulations, a radially-varying exhaust gas is specified at the nozzle exit, consistent with previous studies of plume simulations.[4] This type of boundary condition is not available in the inviscid solver, so plumes are modeled with

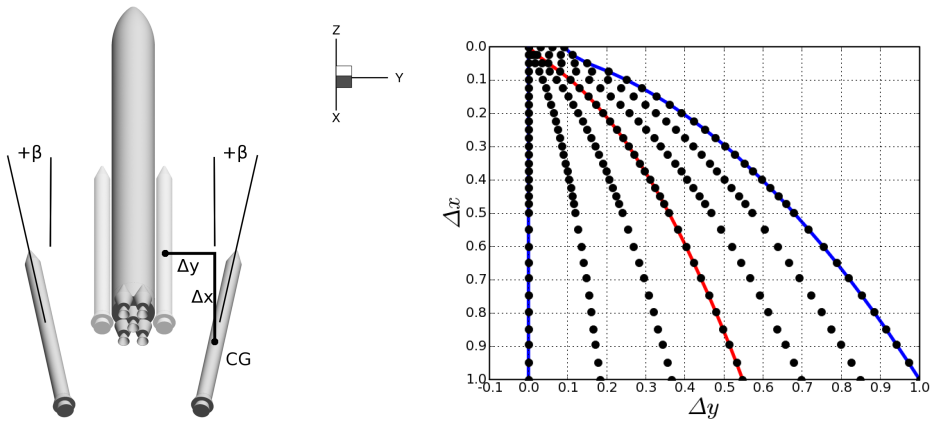

(a) Notation diagram (b) Simulation matrix

Figure 1. (a) SRB orientation relative to initial position, and (b) CFD simulation matrix (black dots), with nominal trajectory (red line), minimum and maximum trajectories (blue lines).

uniform inflow boundary conditions at the nozzle throat, and the flow solver is responsible for producing the correct nozzle exit profile.[7] The Cart3D flow solver is constrained to a single-species perfect gas assumption. Isentropic flow relations are used to adjust the nozzle throat diameter and mean flow nozzle conditions. This is done so that equivalent thrust and mass flow rate conditions are obtained at the exit. The area-ratio of nozzle throat to exit is first computed for a $\gamma = 1.4$ gas,

$$\frac{A_{exit}}{A_{throat}} = \frac{1}{M_{exit}} \left[\frac{2}{\gamma+1} + \frac{\gamma-1}{\gamma+1} M_{exit}^2 \right]^{\frac{\gamma+1}{2(\gamma-1)}}. \tag{1}$$

The sonic conditions are obtained from the following relations:

$$P^* = P_{exit} \left(\frac{1 + \frac{\gamma-1}{2} M_{exit}^2}{1 + \frac{\gamma-1}{2}} \right)^{\frac{\gamma}{\gamma-1}}, \tag{2}$$

$$\rho^* = \rho_{exit} \left(\frac{1 + \frac{\gamma-1}{2} M_{exit}^2}{1 + \frac{\gamma-1}{2}} \right)^{\frac{1}{\gamma-1}}, \tag{3}$$

$$V^* = c^* = \sqrt{\frac{\gamma P^*}{\rho^*}}. \tag{4}$$

The nozzle geometry is cut short at a location that provides the appropriate area ratio, and the computed choke conditions P^*, ρ^*, and V^* are applied uniformly.

III. Computational Method

The approach of the present work is to compute the database using the inviscid flow solver Cart3D, then perform point checks of the solutions with the viscous CFD code OVERFLOW. This avoids the unreasonable computational cost of a viscous database, while still maintaining confidence in the overall validity of the database results.

Cart3D

Database simulations are performed with Cart3D,[8] a NASA-developed inviscid flow solver using an unstructured Cartesian cut-cell approach. One of this software's distinctive features is its functional-dependent

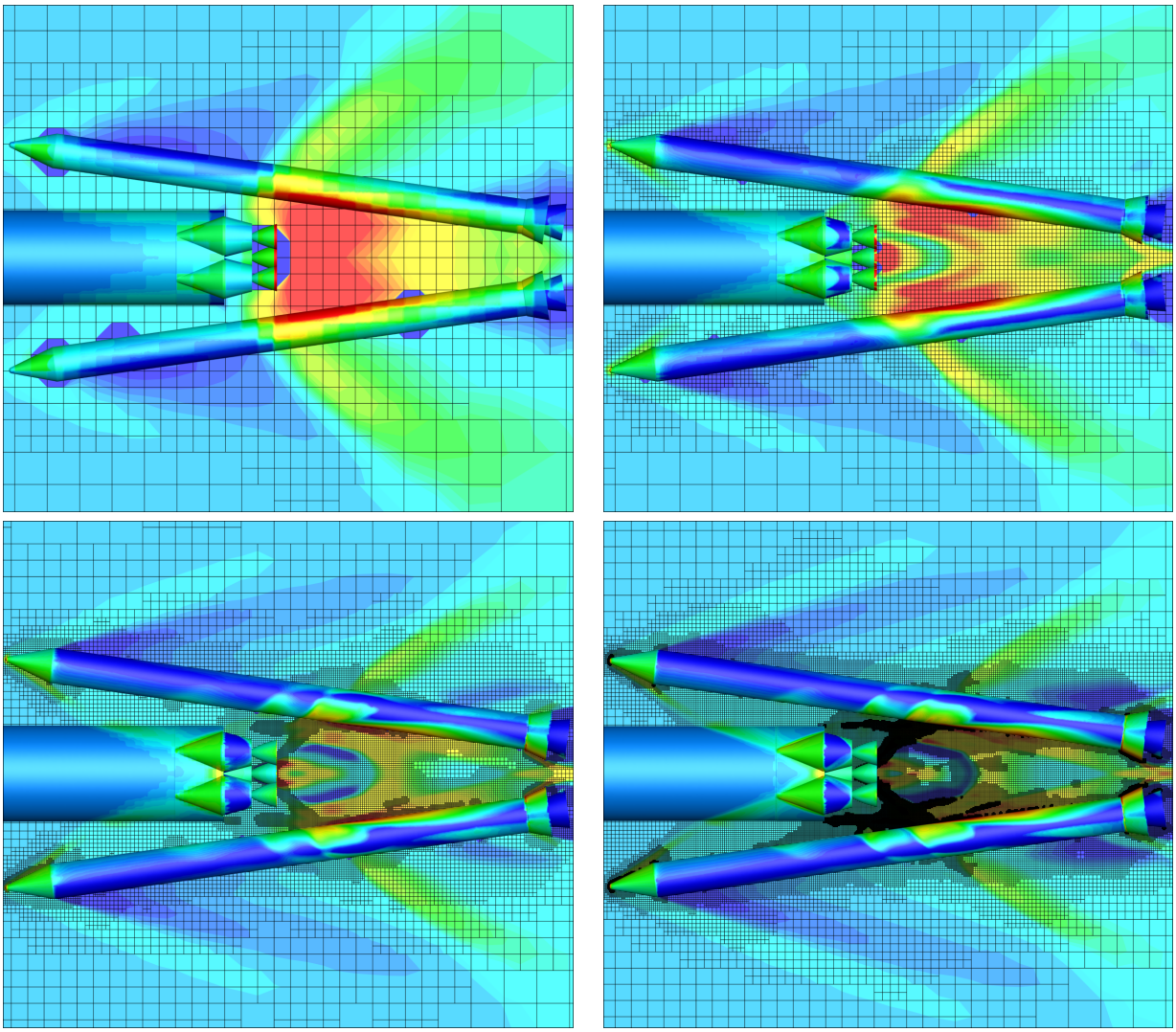

Figure 2. Cart3D grid adaption sequence. Color indicates pressure level (red highest, blue lowest).

adjoint-based adaptive meshing algorithm,[9] which enables accurate and efficient computations for engineering quantities of interest. The functional specified for the present computations is the sum of the forces and moments on the SRBs. The finest resolution attained is 2.54 cm, with total cell counts between 3 and 10 million cells. Computation time for each run was approximately 1 hour using 48 processors of the Columbia supercomputer at the NASA Ames Research Center. A sample solution in Figure 3(a) shows mesh lines on a slice through the flow domain, while an example of the adaption process is illustrated in Figure 2. Mesh refinement concentrates on shocks, plume boundaries, and near the geometry to improve the functional's accuracy. Non-influential regions remain unrefined.

OVERFLOW

OVERFLOW is a viscous Reynolds Averaged Navier-Stokes (RANS) flow solver for structured overset grid systems.[10,11] Solver validation work has been performed on a wide variety of problems, including launch vehicle ascent and plume simulations for the Space Shuttle and the Constellation programs. The present results were computed with second-order central differencing and explicit scalar artificial dissipation using the default dissipation coefficients. Both the Shear Stress Transport (SST) and Spalart-Allmaras (SA) turbulence models are included in the point checking procedure. A diagonalized implicit solver is used and the code is run in parallel using domain decomposition with the Message Passing Interface (MPI) standard

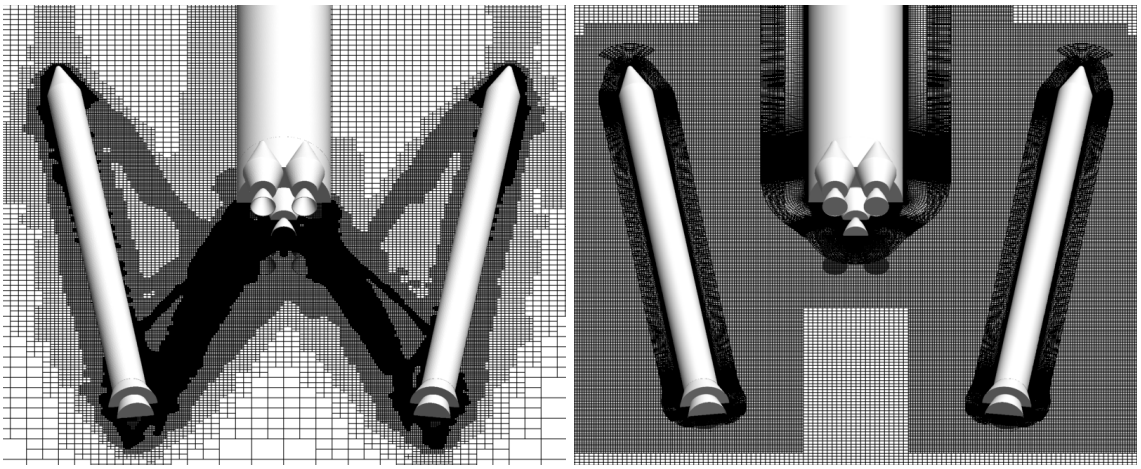

(a) (b)

Figure 3. Slice through (a) an adaptively refined Cartesian grid system for Cart3D, and (b) a viscous overset grid system for OVERFLOW. SRB orientation is the nominal-Δy trajectory at Δx =0.5 and $\beta = 8$ degrees.

for parallel communication. The reported results were run on the Pleiades supercomputer at NASA Ames Research Center, using 256 processors and approximately 20 hours of runtime for each steady-state run. The structured curvilinear viscous overset near-body grid systems were built with grid generation scripts.[12] OVERFLOW's automatic 'bricks' grids are used to create the off-body domain. A slice through the grid system is shown in Figure 3(b).

IV. Results and Analysis

The SRB separation simulations reveal expected trends in the F&M database. If the SRBs stay outside of the core-stage exhaust plume, the forces are consistent with freestream flow effects. Conversely, if the SRBs are not ejected a sufficient distance from the core stage, the exhaust plume impinges first on the aft-section of the SRBs and causes the nose to rotate towards the core. If the SRBs fall straight back, the high-pressure plume will force the SRBs away from the core.

Inviscid Database

Pressure contours of individual flow fields reveal the shock structure, plume expansion, and regions where the highest pressure force is exerted on the SRBs. In Figure 4, streamlines and non-dimensional pressure are plotted for a subset of the non-rotated orientations. The left, middle, and right columns respectively follow the minimum-Δy , nominal, and maximum-Δy trajectories. The top, middle, and bottom rows track locations Δx =0.0, 0.5, and 1.0 downstream. The Δx =0.0 positions show minimal plume interaction with the SRBs, but the reflected bow shocks and proximity to the core stage create higher pressures on the inward sides of the SRBs. At the Δx =0.5 position in the minimum-Δy and nominal-Δy trajectories, plume impingement is immediately apparent from high pressure regions on the inside aft-sections of the SRBs. At the Δx =1.0 position in the minimum-Δy trajectory, the plume is confined (at z=0) between the forward sections of the SRBs. The maximum-Δy trajectory remains outside of the plume's influence for all Δx positions, and the core stage's only effect on the SRBs is from the bow shock's disruption of the incoming freestream flow.

Carpet plots of force and moment reveal global trends and highlight SRB orientations with peak F&M. Figure 5 contains six carpet plots comprised of axial force (CA), side force (CY), and yaw moment (CLN) for SRB rotations $\beta = 0°$ and $6°$. Each plot contains two 'carpets' that represent the left and right SRB configuration spaces. The carpets cover the Δx and Δy configuration space with the third axis representing the force or moment at that location in the matrix. A high F&M value appears red and elevated, while a low value is blue and lower in the perspective plot. The plot of CA in Figure 5(a) shows consistently low axial force except for a slightly higher region that resembles the plume expansion from Figure 4. At these

locations, the plume is impinging on the forward-facing SRB skirts and increasing the force in the downstream direction. For the rotated $\beta = 6°$ case, overall higher axial forces are observed within the plume-influenced region. The peak force occurs along the minimum-Δy trajectory at the lower Δx values where the plume impinges most forcefully on the SRBs. Several points are missing in the carpet plots because SRB rotations at these locations cause intersections with core stage and are not simulated.

The plots of CY in Figure 5(c) and (d) show two important features. First, side force uniformly pushes the SRBs away from the core, a desired feature for SRB separation. Second, CY magnitude is highest along the minimum-Δy trajectory, and increases with rotation angle β. Higher SRB rotation angles can exploit the natural tendency to separate from the core stage.

The final set of CLN plots in (e) and (f) show neutral yaw moment at the maximum-Δy trajectory and an interesting sign inversion along the minimum-Δy trajectory. Tracing the left SRB along the minimum-Δy trajectory from Δx =0.0 to 0.5, CLN rises from neutral to a maximum, then falls back to neutral and on to its minimum value at Δx =1.0. The high yaw moment from the plume impingement on the aft end causes the SRB to rotate 'nose-in' towards the core stage. As the SRB continues to Δx =0.5, the plume impingement is roughly centered on the SRBs center of gravity and causes no yaw moment. As the SRB approaches Δx =1.0, the plume impinges on the nose and causes the SRB to rotate 'nose-out' away from the core stage. Yaw moments are mirrored in the right-side SRB with same-magnitude, opposite-sign values, with magnitudes increasing with positive rotation angle.

Viscous Sensitivity Study

Before viscous solutions are used to point check the inviscid database, a grid convergence study is conducted with OVERFLOW. Only the off-body grids are refined to verify that the resolution is sufficient to accurately propagate the plumes downstream. The resolution of the near-body grids are held fixed with $y^+ = 1$ wall spacing. A series of off-body spacings are applied to the nominal separation event at Δx translations of 0.5 and 1.0. Convergence with grid resolution is shown in Figure 6, where integrated forces on the SRBs are compared to the solution using the finest grid resolution with approximately 120 million grid-points. Solution differences decrease with increasing grid resolution. The SA/SST turbulence models are used on each grid system. The SST model is generally accepted as the more accurate of these two turbulence models for plume simulations, and is chosen for subsequent comparisons. From Figure 6, the SST model shows convergence in X and Y forces to within 4% of the finest mesh when using the 40 million grid-point system, while the results with SA are within 2%.

Inviscid-Viscous Comparison

The inviscid and viscous simulations are compared at Δx =0.25, 0.5, & 1.0 in the minimum-, nominal-, and maximum-Δy trajectories. Figure 7 shows one comparison of streamlines and pressure contours for OVERFLOW and Cart3D. The images show similar qualitative flow patterns, including shock and plume expansion angles, while base pressure is slightly higher in the inviscid solution.

A quantitative comparison of the integrated forces on a single SRB is shown in Figure 8. The difference between Cart3D and OVERFLOW forces is normalized by the respective maximum OVERFLOW force. Forces in the Y-direction differ by less than 10% for all translations and rotations. The majority of forces in the X-direction follow the same 10% trend. The nominal-Δy trajectory at Δx =0.25 and $\beta = 0$ and 8 degrees have the largest differences. In these orientations, the plume impinges on a small part of the SRB's aft end. Small differences in plume expansion angle will have a large impact on the high-pressure region on the forward-facing frustum of the SRB. The difference between the $\gamma = 1.4$ perfect gas assumption used in Cart3D and the multi-species gas assumption of OVERFLOW could be one cause of the difference in plume expansion.

V. Summary

An engineering approach has been presented for database generation of aerodynamic force and moment coefficients on SRBs during separation from a HLLV. The approach balances accuracy and affordability by computing database solutions with the inviscid flow solver Cart3D. Point checking solutions with the viscous RANS solver OVERFLOW is used as a verification procedure for the database. Good agreement with viscous simulations has confirmed that the single-species and inviscid assumptions are valid for this

plume impingement flow, with all simulations within 10-15% of the viscous multi-species results. A simulation matrix is developed across minimum, nominal, and maximum expected trajectories, with 3 degrees of freedom in planar translation and rotation. The database outlines the axial forces, side forces, and yaw moments that are expected downstream of the core stage. Plume impingement causes the highest forces and moments along the minimum-Δy trajectory with high rotation angles, while the maximum-Δy trajectory completely avoids the plume. The location of plume impingement on the SRBs determines the yaw moment, which can range from the dangerous 'nose-towards' the core to a safer 'nose-away' position. Side forces from the plumes help to push the SRBs away from the core stage.

A balance of fidelity and cost has been demonstrated with the engineering approach to database generation. In the initial stages of launch vehicle design, the highest accuracy solutions are unnecessary and even obstructive to design decisions. At this point, a wide range of medium-fidelity analyses are more valuable than a limited number of the highest-fidelity solutions. Development efforts for future HLLVs can benefit from this approach, and better vehicle designs can be achieved by broadening the scope of computational analyses and reducing the turn-around time.

Acknowledgments

The authors would like to acknowledge the outstanding guidance and support from the Cart3D development team, members of the Ares Aero Panel for discussions surrounding this work.

References

[1]Kiris, C., Housman, J., Gusman, M., Chan, W., and Kwak, D., "Time-Accurate Computational Analysis of the Flame Trench Applications," *21st Intl. Conf. on Parallel Computational Fluid Dynamics*, 2009, pp. 37–41.

[2]Gomez, R., Vicker, D., Rogers, S., Aftosmis, M., Chan, W., Meakin, R., and Murman, S., "STS-107 Investigation Ascent CFD Support," *34th AIAA Fluid Dynamics Conference and Exhibit, Portland, Oregon*, June 28 - July 1, 2004, AIAA-2004-2226.

[3]Kiris, C., Housman, J., Gusman, M., Schauerhamer, D., Deere, K., Elmiligui, A., Abdol-Hamid, K., Parlette, E., Andrews, M., and Blevins, J., "Best Practices for Aero-Database CFD Simulations of Ares V Ascent," *AIAA*, January 2011, AIAA-2011-0016.

[4]Gusman, M., Housman, J., and Kiris, C., "Best Practices for CFD Simulations of Launch Vehicle Ascent with Plumes - OVERFLOW Perspective," *49th AIAA Aerospace Sciences Meeting, Orlando, Florida*, Jan 4–7 2011, AIAA–2011–1054.

[5]Chaderjan, N. M., Rogers, S. E., Aftosmis, M. J., Pandya, S. A., Ahmad, J. U., and Tejnil, E., "Automated Euler and Navier-Stokes Database Generation for a Glide-Back Booster," *Computational Fluid Dynamics 2004*, edited by C. Groth and D. W. Zingg, Springer Berlin Heidelberg, 2006, pp. 251–256.

[6]Murman, S. and Aftosmis, M., "Dynamic Analysis of Atmospheric-Entry Probes and Capsules," *45th AIAA Aerospace Sciences Meeting and Exhibit, Reno, Nevada*, Jan 2007, AIAA 2007-74.

[7]Pandya, S., Murman, S., and Aftosmis, M., "Validation of Inlet and Exhaust Boundary Conditions for a Cartesian Method," *22nd AIAA Applied Aerodynamics Conference, Providence, RI*, August 16–19 2004, AIAA–2004–4837.

[8]Aftosmis, M., Berger, M., and Adomavicius, G., "A Parallel Multilevel Method for Adaptively Refined Cartesian Grids with Embedded Boundaries," *38th Aerospace Sciences Meeting and Exhibit, Reno, NV*, Jan 2000, AIAA–2000–0808.

[9]Nemec, M. and Aftosmis, M., "Adjoint Error Estimation and Adaptive Refinement for Embedded-Boundary Cartesian Meshes," *18th AIAA Computational Fluid Dynamics Conference, Miami, Florida*, June 2007, AIAA–2007–4187.

[10]Nichols, R., Tramel, R., and Buning, P., "Solver and Turbulence Model Upgrades to OVERFLOW 2 for Unsteady and High-Speed Applications," *24th AIAA Applied Aerodynamics Conference, San Francisco, California*, June 2006, AIAA–2006–2824.

[11]Nichols, R. and Buning, P., "User's Manual for OVERFLOW 2.1," Version 2.1t.

[12]Pandya, S., Chan, W., and Kless, J., "Automation of Structured Overset Mesh Generation for Rocket Geometries," *19th AIAA Computational Fluid Dynamics Conference, San Antonio, Texas*, Jun 22–25 2009, AIAA–2009–3993.

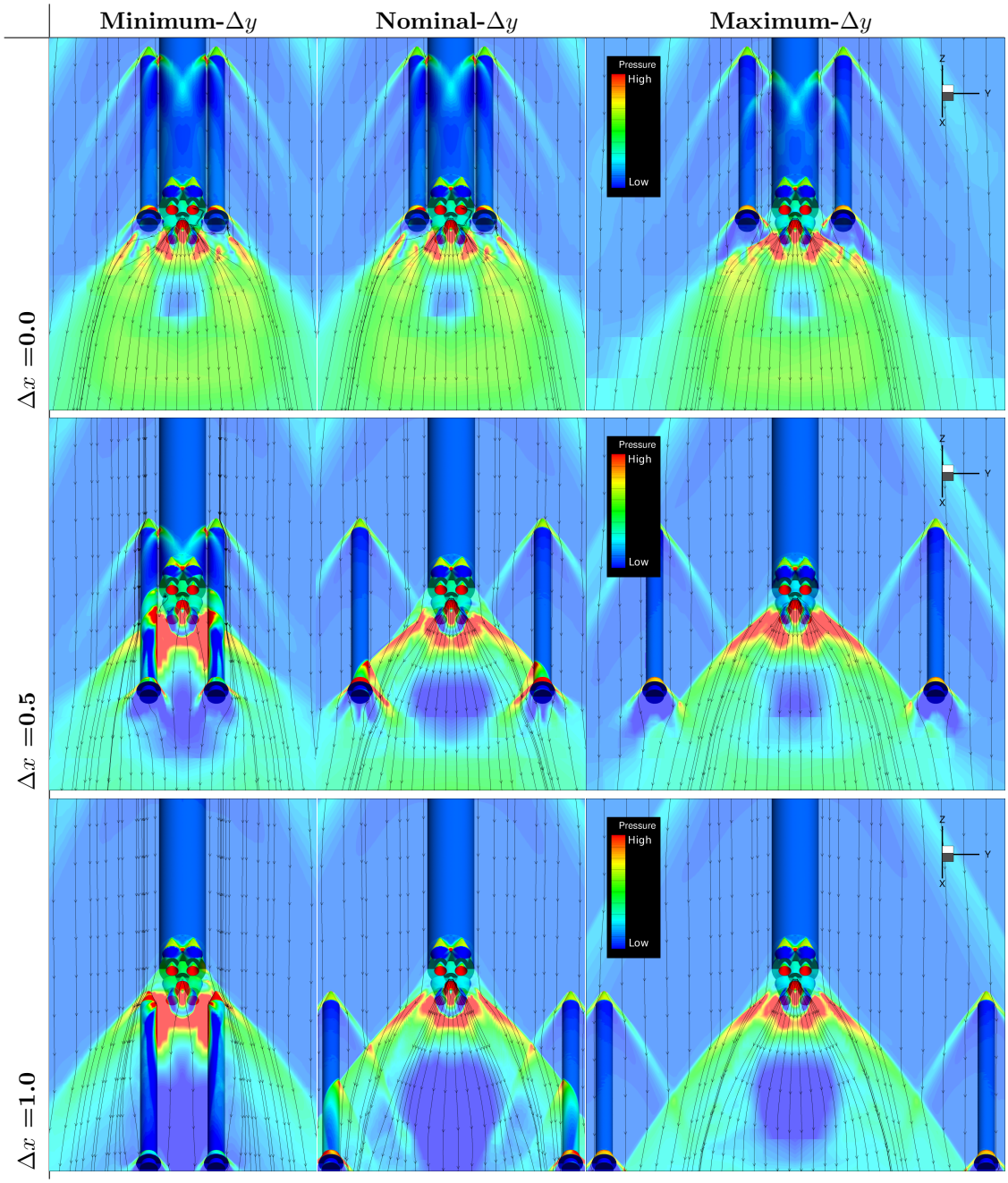

Figure 4. Streamlines and non-dimensional pressure on a slice through the domain and the geometry surfaces.

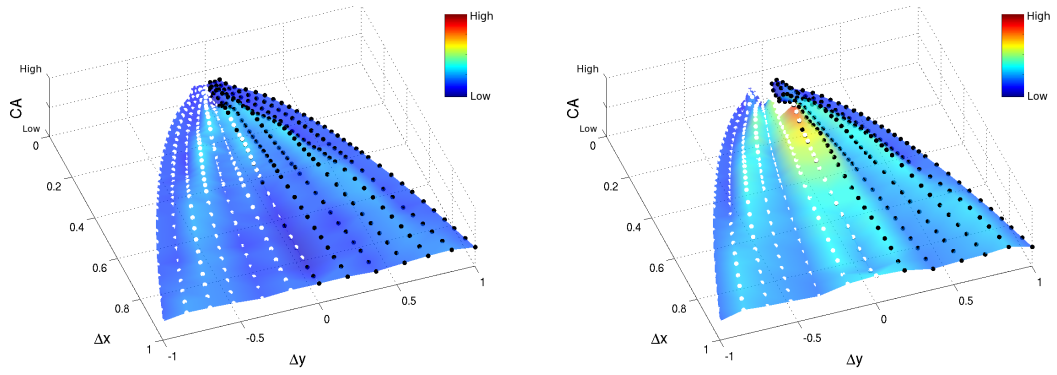

(a) CA, $\beta = 0°$

(b) CA, $\beta = 6°$

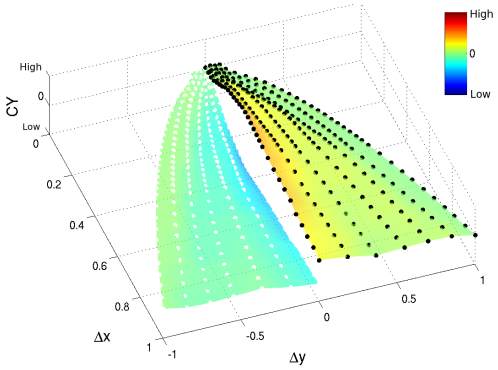

(c) CY, $\beta = 0°$

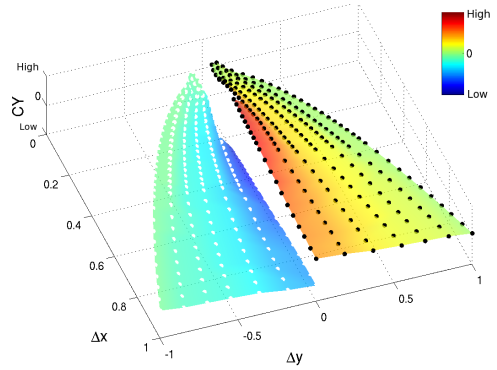

(d) CY, $\beta = 6°$

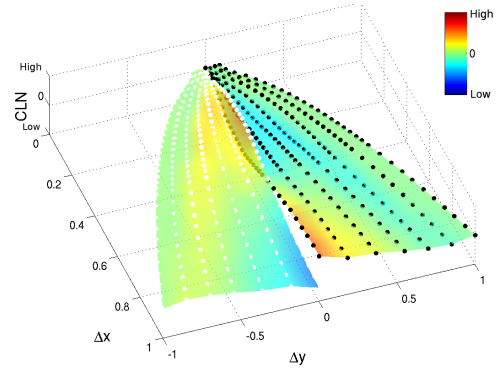

(e) CLN, $\beta = 0°$

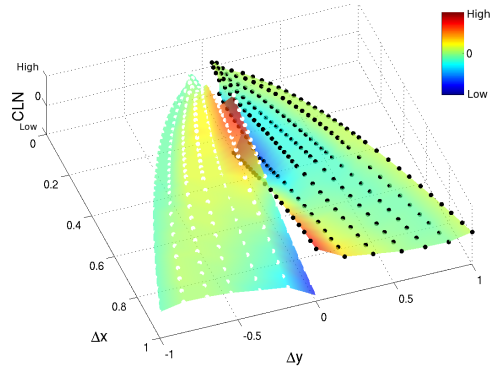

(f) CLN, $\beta = 6°$

Figure 5. Carpet plots of force and moment across simulation martrix, left-side SRB (white dots) and right-side SRB (black dots). Force and moment coefficients normalized by respective maximum values.

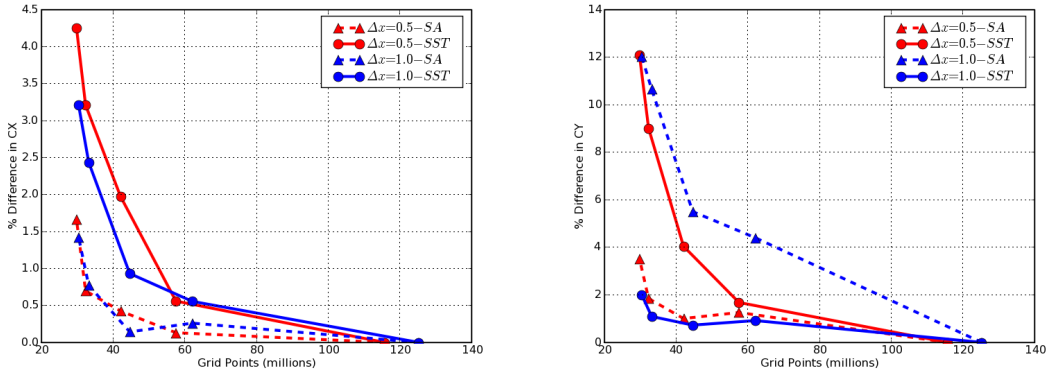

(a) (b)

Figure 6. Grid convergence of OVERFLOW's viscous overset grid system for Δx translations of 0.5 and 1.0, (a) X force, and (b) Y force on right-side SRB.

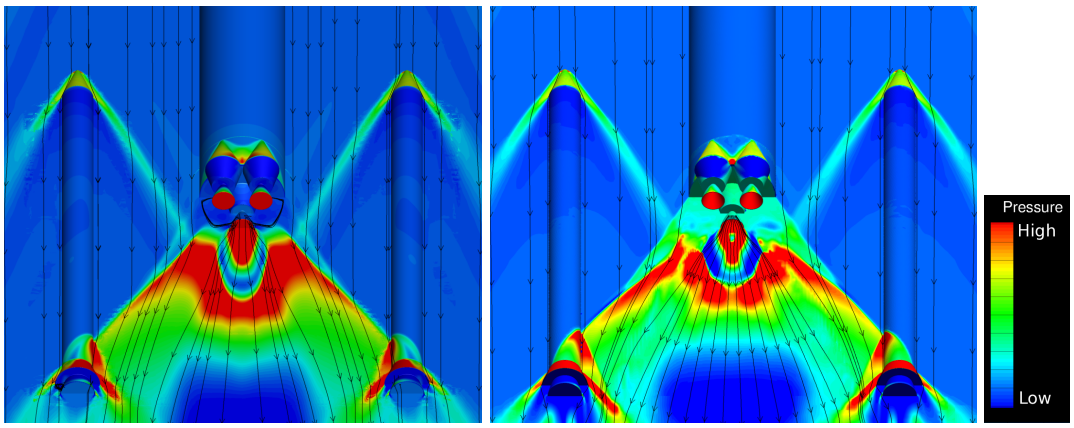

(a) OVERFLOW viscous solution (b) Cart3D inviscid solution

Figure 7. Streamlines and pressure contours on a slice through the fluid domain at Δx =0.5 in the nominal-Δy trajectory at $\beta = 0°$.

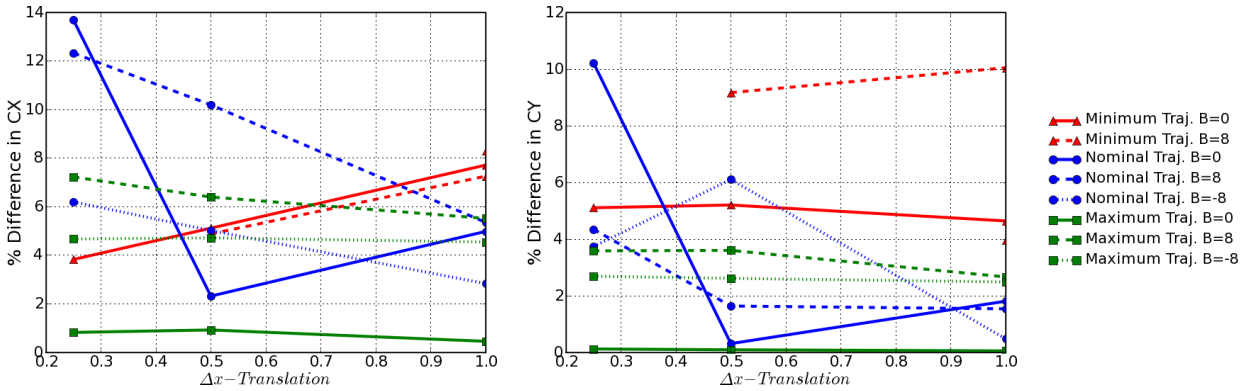

(a) (b)

Figure 8. Difference between OVERFLOW and Cart3D results, (a) X force and (b) Y force on the right-side SRB, with the maximum OVERFLOW force as reference.